

# We are IntechOpen, the world's leading publisher of Open Access books Built by scientists, for scientists

4,800

Open access books available

122,000

International authors and editors

135M

Downloads

Our authors are among the

154

Countries delivered to

TOP 1%

most cited scientists

12.2%

Contributors from top 500 universities



WEB OF SCIENCE™

Selection of our books indexed in the Book Citation Index  
in Web of Science™ Core Collection (BKCI)

Interested in publishing with us?  
Contact [book.department@intechopen.com](mailto:book.department@intechopen.com)

Numbers displayed above are based on latest data collected.  
For more information visit [www.intechopen.com](http://www.intechopen.com)



---

# Surface Plasmonics and Its Applications in Infrared Sensing

---

Guiru Gu, Xuejun Lu, Thitikorn Kemsri and  
Yingjie Zhang

Additional information is available at the end of the chapter

<http://dx.doi.org/10.5772/67410>

---

## Abstract

Surface plasmonic waves have been extensively researched due to their strong surface confinement. The strong surface confinement allows high absorption in an infrared (IR) detector with a thin active absorption region. The excitation of surface plasmonic resonance (SPR) depends on the metallic structures and the interface materials. This enables engineering of plasmonic-enhanced IR detector properties (e.g. detection wavelength, polarization and angular dependence) by properly designing the plasmonic structures. This chapter first gives a brief review of the surface plasmonic waves, followed by the description of SPR excitation in a metallic two-dimensional (2D) sub-wavelength hole array (2DSHA) structure. The applications of the 2DSHA SPR in IR detector enhancement are then presented with a discussion of the polarization and angular dependence.

**Keywords:** surface plasmonic waves, quantum dot, infrared detection

---

## 1. Introduction

Surface electromagnetic waves (also called surface plasmon polaritons, SPPs), predicted by Ritchie in 1957 [1], are coherent electron oscillations at a metal surface. The coherent electron oscillations generate electromagnetic (EM) waves that travel along the dielectric/metal interface [2]. Depending on the metal structures, certain resonant modes of the surface electromagnetic waves can be strongly absorbed (or excited) [2]. This is generally referred to as excitation of surface plasmonic resonance (SPR) modes. SPRs propagate along the metal-dielectric interface. The intensity profile exponentially decreases with the distance from metal-dielectric

interface, that is, SPs are confined at the metal-dielectric interface. Such surface confinement effects have been used in Raman scattering, that is, surface-enhanced Raman scattering (SERS) [3–5] and spectroscopy [6, 7] and have been reported with thousands of times sensitivity enhancement [3, 4]. In addition to SERS, the SPR enhancement technology also provides a promising technique to concentrate EM energy on surface area and thus enables high quantum efficiency with a thin active absorption layer in a photodetector. Significant performance enhancements in a quantum dot infrared photodetector (QDIP) have been reported [8–15].

In addition, the SPR modes can also change EM field distribution and thus offers an effective technique for EM field engineering to achieve specific transmission and/or receiving patterns with polarization and detection spectrum engineering capability [11, 16]. In this chapter, a brief review of the fundamental concepts of SPRs will be first given and followed by the description of their applications in infrared detections. SPR-based EM field engineering will also be presented with the discussion of polarization and receiving angle control.

## 2. Review of surface plasmonic resonance

### 2.1. Plasma frequency, complex conductivity and the Drude model

Plasmonic waves are electromagnetic waves. They follow Maxwell equations, which can be expressed as follows in the phasor domain

$$\nabla \cdot \vec{D} = \rho, \quad (1)$$

$$\nabla \times \vec{E} = -j\omega\mu\vec{H}, \quad (2)$$

$$\nabla \cdot \vec{B} = 0, \quad (3)$$

$$\nabla \times \vec{H} = \vec{J} + j\omega\epsilon\vec{E}, \quad (4)$$

where  $\vec{J}$  is the current density,  $\vec{D}, \vec{E}$ , are the electric flux density and the electric field, respectively, and  $\vec{B}, \vec{H}$  are the magnetic flux density and the magnetic field, respectively,  $\omega$  is the angular frequency, and  $\epsilon$  and  $\mu$  are the permittivity and permeability of the material, respectively. The current density  $\vec{J}$  is related to  $\vec{E}$  by:

$$\vec{J} = \sigma\vec{E}, \quad (5)$$

where  $\sigma$  is the conductivity of the material. Eq. (4) can therefore be expressed as follows:

$$\nabla \times \vec{H} = j\omega\epsilon \left( 1 + \frac{\sigma}{j\omega\epsilon} \right) \vec{E}, \quad (6)$$

where  $\epsilon_c = \epsilon \left( 1 + \frac{\sigma}{j\omega\epsilon} \right)$  is the complex permittivity of the material. The Maxwell's current continuity equation is as follows:

$$\nabla \cdot \vec{J} = -e \frac{\partial n}{\partial t}, \quad (7)$$

where  $e$  is the charge of an electron,  $e = 1.6 \times 10^{-19}$  (C),  $n$  is the density of electrons in metal.

The current density is related to the speed of the charge  $v$  by:

$$\vec{J} = en_0 v, \quad (8)$$

where  $n_0$  is the average electron density in metal. Combining Eqs. (7) and (8), one gets:

$$n_0 \nabla \cdot \vec{v} = -\frac{\partial}{\partial t} n, \quad (9)$$

Taking another partial derivative of  $t$ , one gets:

$$n_0 \nabla \cdot \frac{\partial \vec{v}}{\partial t} = -\frac{\partial^2}{\partial t^2} n, \quad (10)$$

Eq. (10) can be expressed as follows:

$$\frac{n_0}{m} \nabla \cdot m \vec{a} = -\frac{\partial^2}{\partial t^2} n, \quad (11)$$

where  $m$  is the mass of an electron. The  $m \vec{a}$  term is the force on the electron, which is the electric force,  $\vec{F} = e \vec{E}$ . Eq. (11) can thus be changed to

$$\frac{en_0}{m} \nabla \cdot \vec{E} = -\frac{\partial^2}{\partial t^2} n, \quad (12)$$

In phasor domain, Eq. (12) can be expressed as follows:

$$\frac{en_0}{m} \nabla \cdot \vec{E} = \omega_p^2 n, \quad (13)$$

where  $\omega_p$  is the plasma frequency. Combining Eqs. (1) and (13), one gets

$$\omega_p = \sqrt{\frac{e^2 n_0}{m \epsilon}} \quad (14)$$

Taking the partial derivative of  $t$  for Eq. (8), one gets

$$\frac{\partial \vec{J}}{\partial t} = \frac{en_0}{m} m \frac{\partial}{\partial t} v, \quad (15)$$

The  $m \frac{\partial \vec{v}}{\partial t}$  term can be replaced by the electric force,  $\vec{F} = e \vec{E}$ . Eq. (15) becomes

$$\frac{\partial \vec{J}}{\partial t} = \frac{e^2 n_0}{m} \vec{E}, \quad (16)$$

In phasor domain, Eq. (16) can be rewritten as follows:

$$j\omega \vec{J} = \frac{e^2 n_0}{m} \vec{E}, \tag{17}$$

Combining Eqs. (5) and (17), one gets:

$$\sigma = \frac{e^2 n_0}{j\omega m}, \tag{18}$$

The complex permittivity  $\epsilon_c$  is thus given as follows:

$$\epsilon_c = \epsilon \left( 1 + \frac{\sigma}{j\omega\epsilon} \right) = \epsilon \left( 1 - \frac{e^2 n_0}{\omega^2 m \epsilon} \right) = \epsilon \left( 1 - \frac{\omega_p^2}{\omega^2} \right) \tag{19}$$

The derivations and equations above are for the ideal lossless free-electron gas model. The loss term can be included in the model by introducing a relaxation rate  $\gamma$ , that is,

$$\epsilon_c = \epsilon \left( 1 - \frac{\omega_p^2}{\omega^2 + j\omega\gamma} \right) \tag{20}$$

Eq. (20) is the complex permittivity given by the well-known Drude model [17].

### 2.2. Plasmonic waves at the dielectric and metal interface

Following Raether in Ref. [2], one can analyse plasmonic waves using a transmagnetic (TM) plane wave. **Figure 1** shows the incident of a TM plane EM wave with the  $H$ -field in the  $y$ -direction. Note that the phasor expressions of the  $H$ -fields follow the convention of  $i\vec{k} \cdot \vec{R}$  indicating the wave travels in the  $\vec{R}$  direction, whereas  $-i\vec{k} \cdot \vec{R}$  indicating the wave travels in the  $-\vec{R}$  direction. A negative sign needs to be included in Eq. (6) to use this convention.

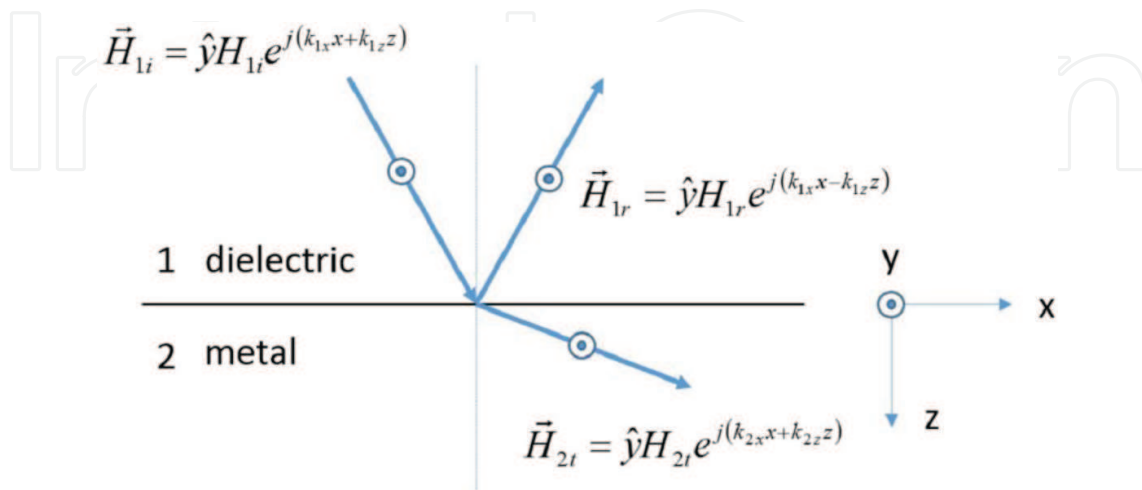


**Figure 1.** Scheme of TM wave incidence at the dielectric and metal interface.

Under the aforementioned convention, the E-field defined by Eq. (6) can be changed to

$$\vec{E} = -\frac{1}{j\omega\epsilon_c} \nabla \times \vec{H} \quad (21)$$

From Eq. (21), the  $E_x$  can be expressed as follows:

$$\vec{E}_{1i} = -\hat{x} \frac{jk_{1z}}{j\omega\epsilon_1} H_{1i} e^{j(k_{1x}x+k_{1z}z)} \quad (22)$$

$$\vec{E}_{1r} = \hat{x} \frac{jk_{1z}}{j\omega\epsilon_1} H_{1r} e^{j(k_{1x}x-k_{1z}z)} \quad (23)$$

$$\vec{E}_{2t} = -\hat{x} \frac{jk_{2z}}{j\omega\epsilon_{2c}} H_{2t} e^{j(k_{2x}x+k_{2z}z)} \quad (24)$$

where  $k_{1x}$ ,  $k_{1z}$  are the x and z components of the propagation constant  $k_1$ , respectively. Similarly,  $k_{2x}$ ,  $k_{2z}$  are the x and z components of the propagation constant  $k_2$ , respectively.

$$k_{1x}^2 + k_{1z}^2 = k_1^2 = \omega^2 \epsilon_1 \mu_1 \quad (25)$$

$$k_{2x}^2 + k_{2z}^2 = k_2^2 = \omega^2 \epsilon_{2c} \mu_2 \quad (26)$$

where  $\mu_1 \approx \mu_2 \approx \mu_0$  are the permeability of the material 1, 2 and vacuum, respectively. The boundary conditions are  $H_y$  and  $E_x$  continuous at the interface (i.e.  $z = 0$ ). Applying the boundary conditions, one gets the following:

$$H_{1i} e^{jk_{1x}x} + H_{1r} e^{jk_{1x}x} = H_{2t} e^{jk_{2x}x} \quad (27)$$

$$\frac{k_{1z}}{\epsilon_1} H_{1i} e^{jk_{1x}x} - \frac{k_{1z}}{\epsilon_1} H_{1r} e^{jk_{1x}x} = \frac{k_{2z}}{\epsilon_{2c}} H_{2t} e^{jk_{2x}x} \quad (28)$$

Since Eq. (27) and Eq. (28) are valid for any  $x$ ,  $k_{1x} = k_{2x}$ .

When there is no reflection, that is,  $H_{1r} = 0$ , Eqs. (27) and (28) become

$$H_{1i} = H_{2t} \quad (29)$$

$$\frac{k_{1z}}{\epsilon_1} H_{1i} = \frac{k_{2z}}{\epsilon_{2c}} H_{2t} \quad (30)$$

Combining Eqs. (29) and (30), one gets the following:

$$k_{2z} = \epsilon_{2c} \frac{k_{1z}}{\epsilon_1} \quad (31)$$

Plugging Eq. (31) into Eq. (26), one gets the following:

$$k_{2x}^2 + k_{2z}^2 = \frac{\epsilon_{2c}^2}{\epsilon_1^2} k_{1z}^2 + k_{2x}^2 = \omega^2 \epsilon_{2c} \mu_0 \quad (32)$$

Combing Eq. (32) with Eq. (25), one can get  $k_{1x}$  as follows:

$$k_{1x}^2 = \omega^2 \mu_0 \frac{\epsilon_{2c} \epsilon_1}{(\epsilon_1 + \epsilon_{2c})} \quad (33)$$

Eq. (33) can be expressed using relative permittivity  $\epsilon_{1r}$  and  $\epsilon_{2cr}$ .

$$k_{1x}^2 = \omega^2 \mu_0 \epsilon_0 \frac{\epsilon_{2cr} \epsilon_{1r}}{(\epsilon_{1r} + \epsilon_{2cr})} \quad (34)$$

where  $\epsilon_{1r} = \frac{\epsilon_1}{\epsilon_0}$  and  $\epsilon_{2cr} = \frac{\epsilon_{2c}}{\epsilon_0}$ .

$$k_x = k_0 \text{Re} \left[ \sqrt{\frac{\epsilon_{2cr} \epsilon_{1r}}{(\epsilon_{1r} + \epsilon_{2cr})}} \right] + j k_0 \text{Im} \left[ \sqrt{\frac{\epsilon_{2cr} \epsilon_{1r}}{(\epsilon_{1r} + \epsilon_{2cr})}} \right] \quad (35)$$

$k_{2z}$  can be obtained from Eq. (34) as follows:

$$k_{2z} = k_0 \text{Re} \left[ \sqrt{\frac{\epsilon_{2cr} \epsilon_{2cr}}{(\epsilon_{1r} + \epsilon_{2cr})}} \right] + j k_0 \text{Im} \left[ \sqrt{\frac{\epsilon_{2cr} \epsilon_{2cr}}{(\epsilon_{1r} + \epsilon_{2cr})}} \right] \quad (36)$$

where  $\text{Re}(\cdot)$  and  $\text{Im}(\cdot)$  are taking the real and the imaginary parts. The plasmonic wave propagates in  $x$  and  $z$  directions with loss described by the imaginary parts of the corresponding directions, that is,  $k_{\text{spp}} = k_x$ . Since  $\epsilon_{2cr}$  is generally much larger than  $\epsilon_{1r}$ , Eq. (36) can be simplified as follows:

$$k_x = k_0 \sqrt{\epsilon_{1r}} \quad (37)$$

### 2.3. Plasmonic wave excitation in a metallic two-dimensional (2D) sub-wavelength hole array (2DSHA) structure

Surface plasmonic waves can be excited by numerous structures. The metallic 2DSHA structure [18] is one of the commonly used plasmonic structures for performance enhancement in infrared photodetectors [8, 10–12]. **Figure 2** shows a schematic structure with the light incident scheme of the metallic 2DSHA array structure. The 2DSHA structure is a square lattice with the period of  $p$ , and the diameter of the hole is  $d$ . The periodical structure provides a grating vector of  $\Lambda = \frac{2\pi}{p}$ . Surface plasmonic wave can be excited when the grating vector of  $\Lambda$  matches the  $k_{\text{spp}}$ , that is,  $k_{\text{spp}} = \frac{2\pi}{p}$ .

**Figure 3** shows the cross section of the light incidence on the 2DSHA structure. The excited plasmonic waves and the scattered waves by the 2DSHA structure are indicated in the figure.

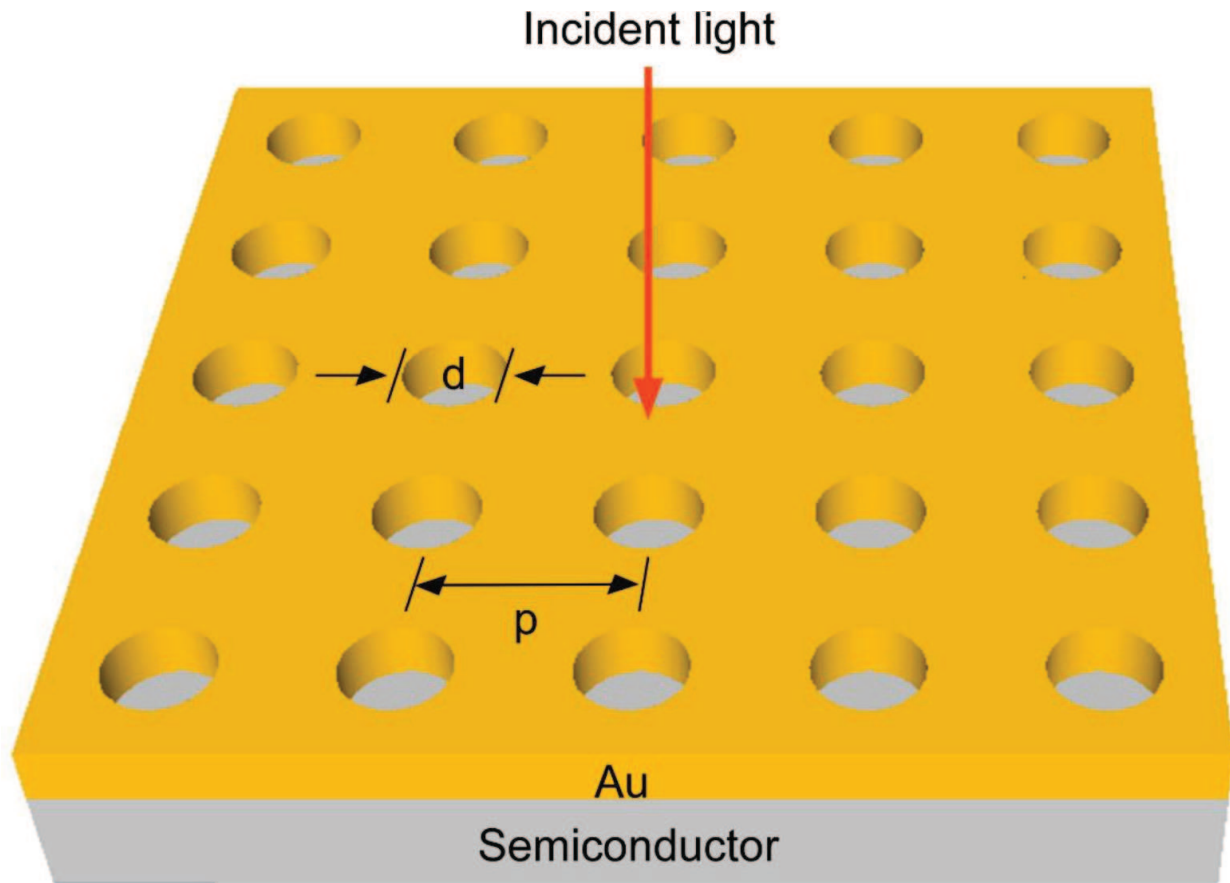


**Figure 2.** Schematic structure with the light incident scheme of the metallic 2DSHA array structure. The 2DSHA structure is square lattice with a period of  $p$ , and the diameter of the hole is  $d$ .

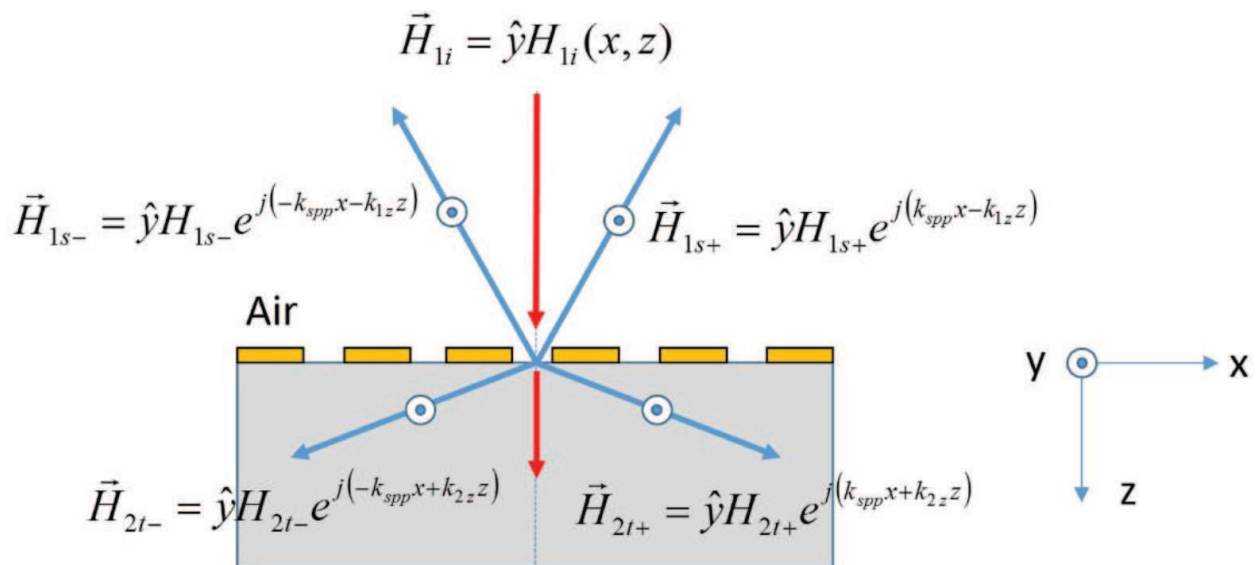


**Figure 3.** Schematic of the cross-section of the light incidence on the 2DSHA structure. The 2DSHA structure generates plasmonic waves and scattering waves.



From E-M field boundary conditions, the following relations hold:

$$H_{1s-} = H_{2t-} \quad (38)$$

$$H_{1s+} = H_{2t+} \quad (39)$$

$$\frac{k_{1z}}{\varepsilon_1} = -\frac{k_{2z}}{\varepsilon_2} \quad (40)$$

The excitation efficiency  $\eta$  can be defined by the overlap integral of the incident field with the plasmonic waves, that is,

$$\eta = \int \mathbf{H}(x, z) e^{i(k_{spp}x + k_{2z}z)} \Big|_{z=0} dx \quad (41)$$

where  $H(x, z)$  is the magnetic field of the incident wave modified by the 2DSHA, that is, the periodical 2DSHA structure will introduce periodical variation in  $H(x, z)$  as well.

#### 2.4. Near-field E-field distribution in the 2DSHA structure

The near-field E-field component can be simulated as well. **Figure 4** shows the top ( $x$ - $y$ ) and cross-section ( $x$ - $z$ ) views of the  $E_x$  component at different wavelengths. The 2DSHA structure is square lattice with a period of  $2.3 \mu\text{m}$ , and the diameter of the hole is  $1.15 \mu\text{m}$ . The simulation is performed using CST Microwave studio<sup>®</sup>. The incident light is linearly polarized surface normal plane wave with E-field magnitude of  $1 \text{ V/m}$ . The colour scale bar represents the magnitude of the  $E_x$ .

**Figure 5** shows the top ( $x$ - $y$ ) and cross-section ( $x$ - $z$ ) views of the  $E_z$  component at different wavelengths. From **Figures 4** and **5**, both  $E_x$  and  $E_z$  strongly depend on the excitation wavelengths.  $E_z$  is high between  $7.6$  and  $8.5 \mu\text{m}$ , whereas  $E_x$  is strong between  $7.6$  and  $8.0 \mu\text{m}$ .  $E_z$  is primarily at the edge of the holes, whereas  $E_x$  is inside the holes. The period of the 2DSHA  $p = 2.3 \mu\text{m}$ ,  $k_{spp} = \frac{2\pi}{p}$ .

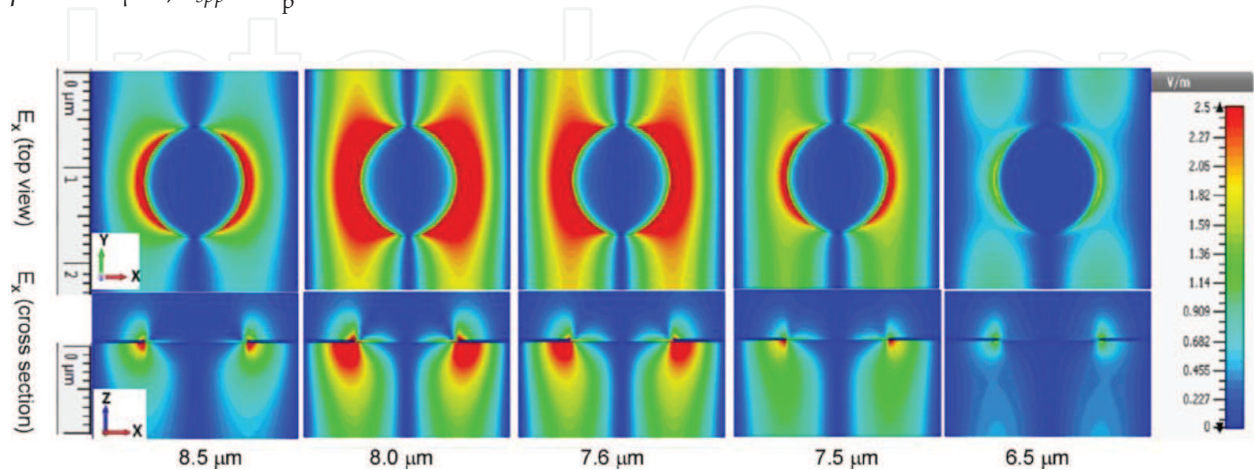


**Figure 4.** Top and cross-section views of the  $E_x$  component at different wavelengths simulated using CST Microwave studio<sup>®</sup>. The incident light is a linearly polarized surface normal plane wave with E-field magnitude of  $1 \text{ V/m}$ .

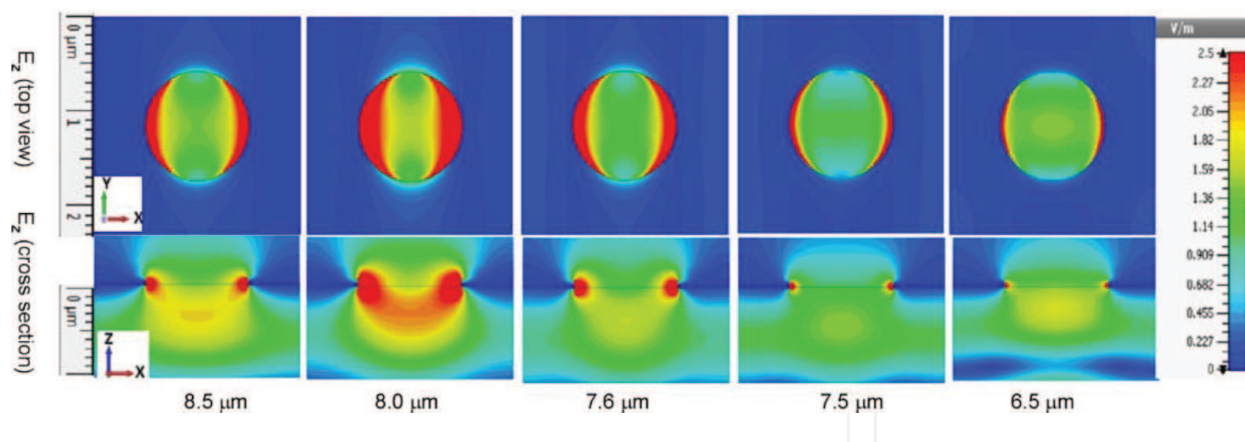


**Figure 5.** Top and cross-section views of the  $E_z$  component at different wavelengths simulated using CST Microwave studio<sup>®</sup>. The incident light and the simulation conditions are the same.

From Eq. (35),  $k_{spp}$  is

$$k_{spp} = \frac{2\pi}{\lambda_0} \text{Re} \left[ \sqrt{\frac{\epsilon_{2cr}\epsilon_{1r}}{(\epsilon_{1r} + \epsilon_{2cr})}} \right] + j \frac{2\pi}{\lambda_0} \text{Im} \left[ \sqrt{\frac{\epsilon_{2cr}\epsilon_{1r}}{(\epsilon_{1r} + \epsilon_{2cr})}} \right] \quad (42)$$

where  $\lambda_0$  is the free space wavelength,  $\epsilon_m$  and  $\epsilon_d$  are the relative permittivity of the metal and GaAs, respectively. The dielectric constant of GaAs in the long-wave infrared region is 10.98 [19]. The dielectric constant of Au is calculated to be  $-1896 + i684$  at  $7.6 \mu\text{m}$  [1]. The calculated plasmonic resonant wavelength is  $\lambda_{sp} = 7.6 \mu\text{m}$ . At the resonant wavelength (i.e.  $\lambda = 7.6 \mu\text{m}$ ), the E-fields are strongly confined near the surface. Such strong surface confinement of plasmonic waves enables high absorption using a thin absorption layer and thus leads to significant enhancement in quantum dot infrared photodetectors (QDIPs) [8, 10–13, 15]. In the following sections, we will first give a brief introduction of QDIPs, followed by the description of surface plasmonic enhancement in QDIPs.

### 3. QDIPs in mid-wave infrared (MWIR) and long-wave infrared (MWIR/LWIR) detection

QDIPs are based on intersubband transitions in self-assembled InAs quantum dots (QDs). The simplified band diagram and the schematic structures of a QD infrared photodetector (QDIP) are shown in **Figure 6(a)** and **6(b)**, respectively. The s, p, d, f, represent the energy levels of a QD with the wetting layers (WL). A typical QDIP consists of vertically-stacked InAs quantum dots layers with GaAs capping layers. The electrons are excited by the normal incident light and subsequently collected through the top electrode and generate photocurrent. This is a unipolar photodetector, where only conduction band is involved in the photodetection and photocurrent generation process.

The QDIP technology offers a promising technology in MWIR and LWIR photodetection due to the advantages provided by the three-dimensional (3D) quantum confinement of

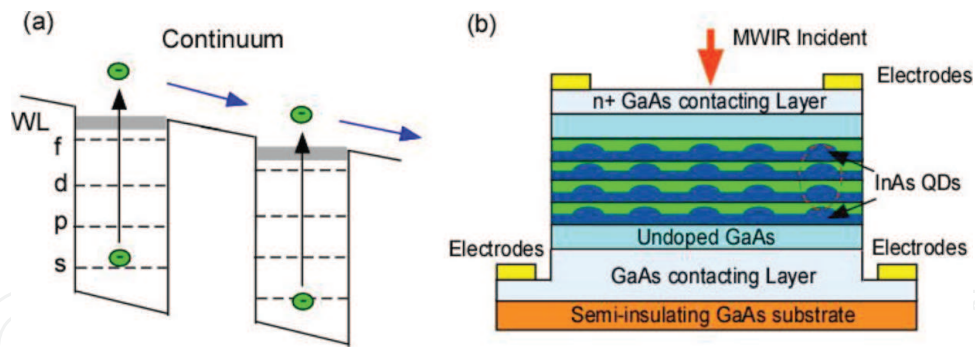


**Figure 6.** Schematic structure of a unipolar QDIP with the intersubband transition: (a) simplified band diagram and (b) schematic of the QDIP. The s, p, d and f, represent the energy levels of a QD.

carriers—including intrinsic sensitivity to normal incident radiation [13], high photoconductive (PC) gain, high quantum efficiency [15] and photoresponsivity [16]. The normal incidence detection capability greatly simplifies the fabrication complexity for a large format ( $1\text{K} \times 1\text{K}$ ) FPA. The high photoconductive (PC) gain and high photoresponsivity provide a promising way for MWIR and LWIR sensing and detection.

**Figure 7** shows the photodetection spectrum of a QDIP. It covers a broadband IR spectrum from 3 to 9  $\mu\text{m}$ . The insert of **Figure 7** shows an atomic force microscopic (AFM) picture of the QDs by self-assembled epi-growth. The growth gives high-density QDs with uniform sizes. The InAs/

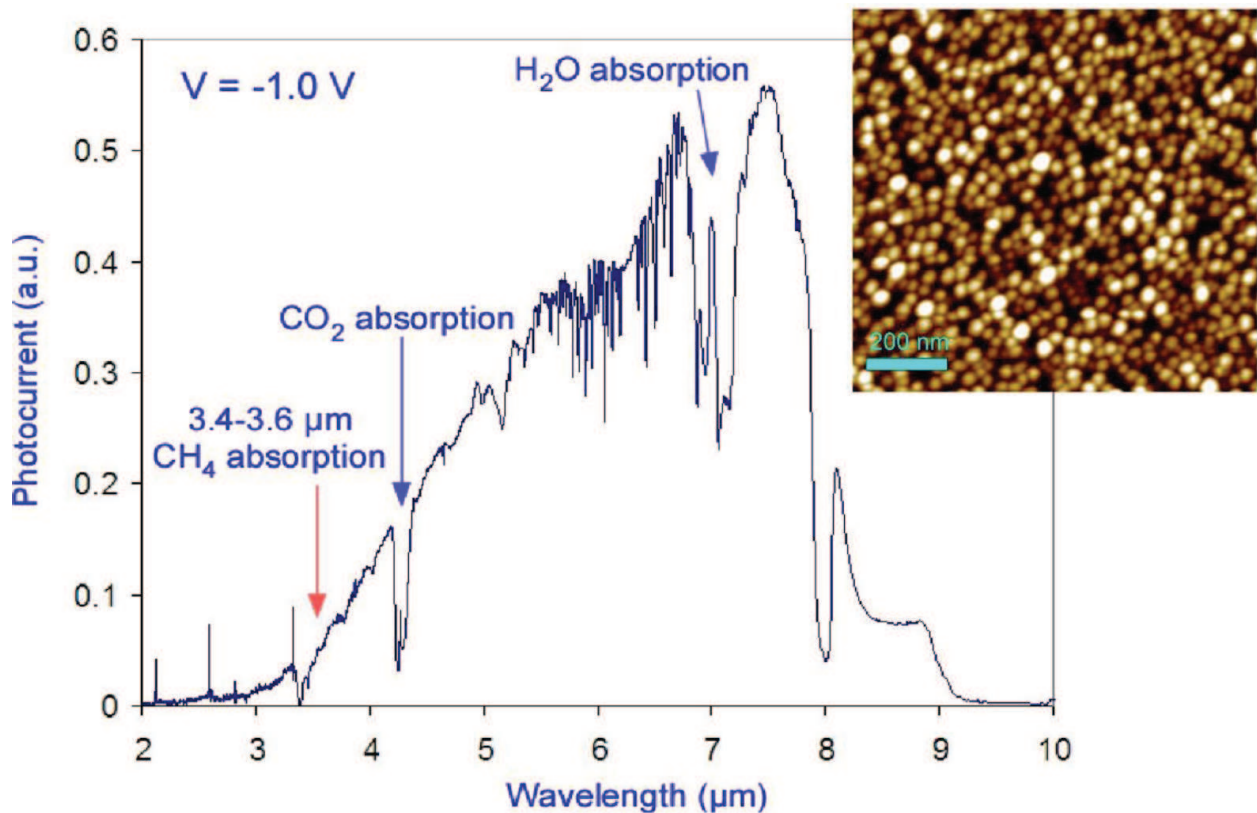


**Figure 7.** Photodetection spectrum of a QDIP. It shows a broad IR detection spectrum from 3 to 9  $\mu\text{m}$ . The insert shows an AFM image of the QDs by self-assembled epi-growth.



GaAs QD material is a mature material system with low substrate cost, high material quality and large wafer growth capability. It can offer low-cost MWIR and LWIR photodetectors and focal plane arrays (FPAs) with simplified fabrication processes and high yield. Detailed QDIP performance, such as photoconductive gains, noise, photoresponsivity and photodetectivity can be found in literature [20–27].

## 4. 2DSHA plasmonic-enhanced QDIPs

### 4.1. Backside configured 2DSHA-enhanced QDIPs

Surface confinement of plasmonic waves enables high absorption using a thin absorption layer and thus leads to significant enhancement in QDIPs [8, 10–13, 15]. We have developed a backside-configured plasmonic enhancement technology by fabricating the 2DSHA plasmonic structures on top of a QDIP and illuminating the QDIP from the opposite side of the plasmonic structure (i. e. backside illumination) [12]. **Figure 8(a)** and **8(b)** show the schematic cross-section structures of the backside-configured plasmonic QDIP and the reference QDIP without the

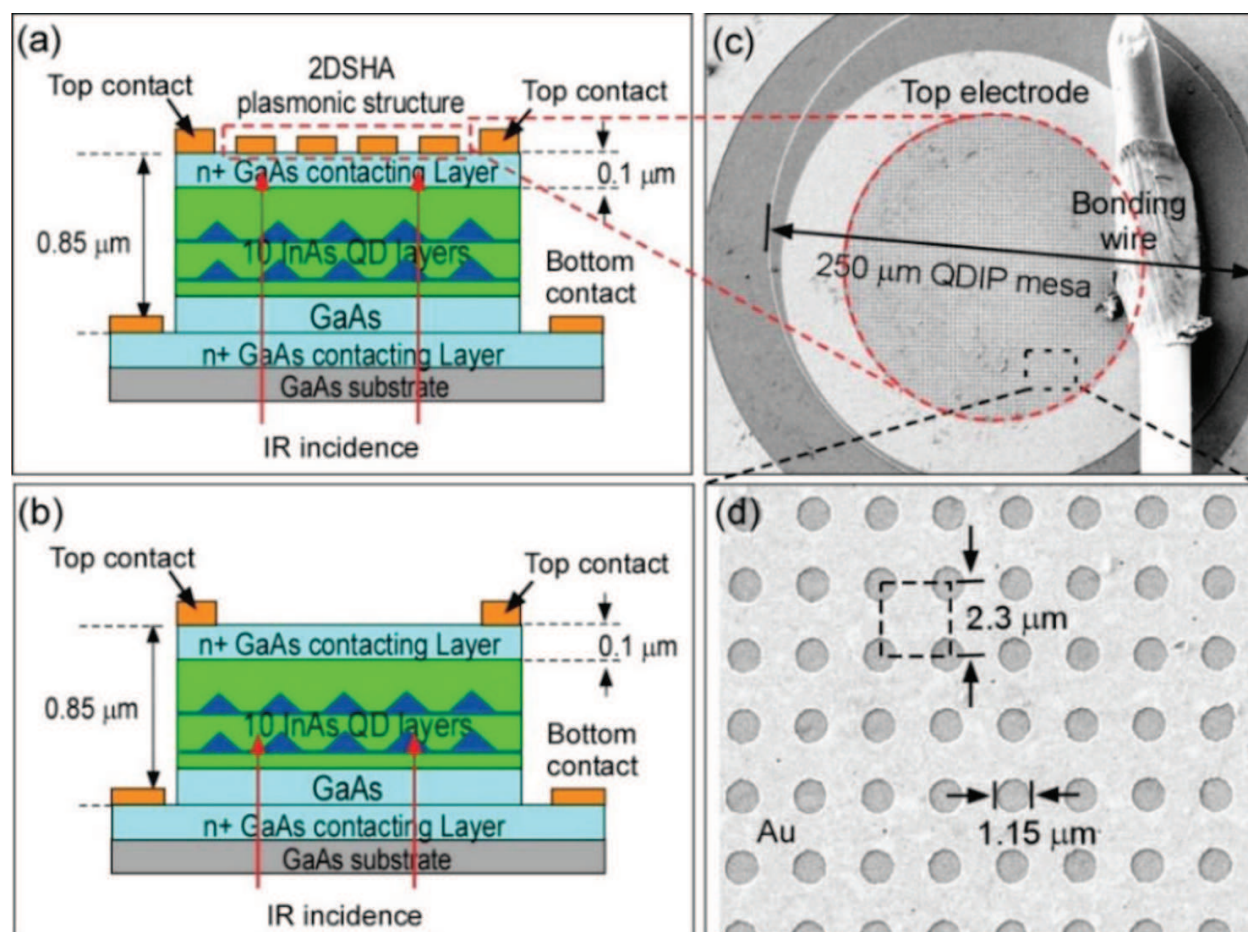


**Figure 8.** (a) Schematic cross-section structure of the backside-configured 2DSHA plasmonic structure on the QDIP. The IR incident light illuminates from the substrate side; (b) ref-QDIP without the plasmonic structure; (c) SEM image of the 2DSHA plasmonic structure on the QDIP and (d) close-up view of the plasmonic structure (© IOP Publishing. Reproduced with permission from Ref. [12]. All rights reserved).

plasmonic structure, respectively. **Figure 8(c)** and **8(d)** show scanning electron microscopic (SEM) images of the plasmonic structures on a QDIP and a close-up view of the plasmonic structure, respectively.

**Figure 9** shows the measured photocurrent spectra of the backside-configured plasmonic QDIP compared with the top-side configured plasmonic QDIP and the reference QDIP. The backside-configured plasmonic QDIP clearly shows higher plasmonic enhancement than those of the top-side configured plasmonic QDIP and the reference QDIP.

**Figure 10(a)** shows the simulated E-field intensities of the top and backside-configured plasmonic structures, respectively. The backside-configured plasmonic structure can induce stronger E-field at the interface and therefore can provide larger plasmonic enhancement [12].

#### 4.2. Wavelength-tuning and multispectral enhancement

From Eq. (42) and  $k_{spp} = \frac{2\pi}{p}$ , one gets:

$$\lambda_{sp} = \frac{p}{\sqrt{m^2 + n^2}} \operatorname{Re} \left[ \sqrt{\frac{\epsilon_{2cr}\epsilon_{1r}}{(\epsilon_{1r} + \epsilon_{2cr})}} \right] \quad (43)$$

where (m, n) are the orders of the grating vectors. Therefore, the plasmonic resonance wavelength can be tuned by changing the period of the 2DSHA plasmonic structure. The plasmon resonant

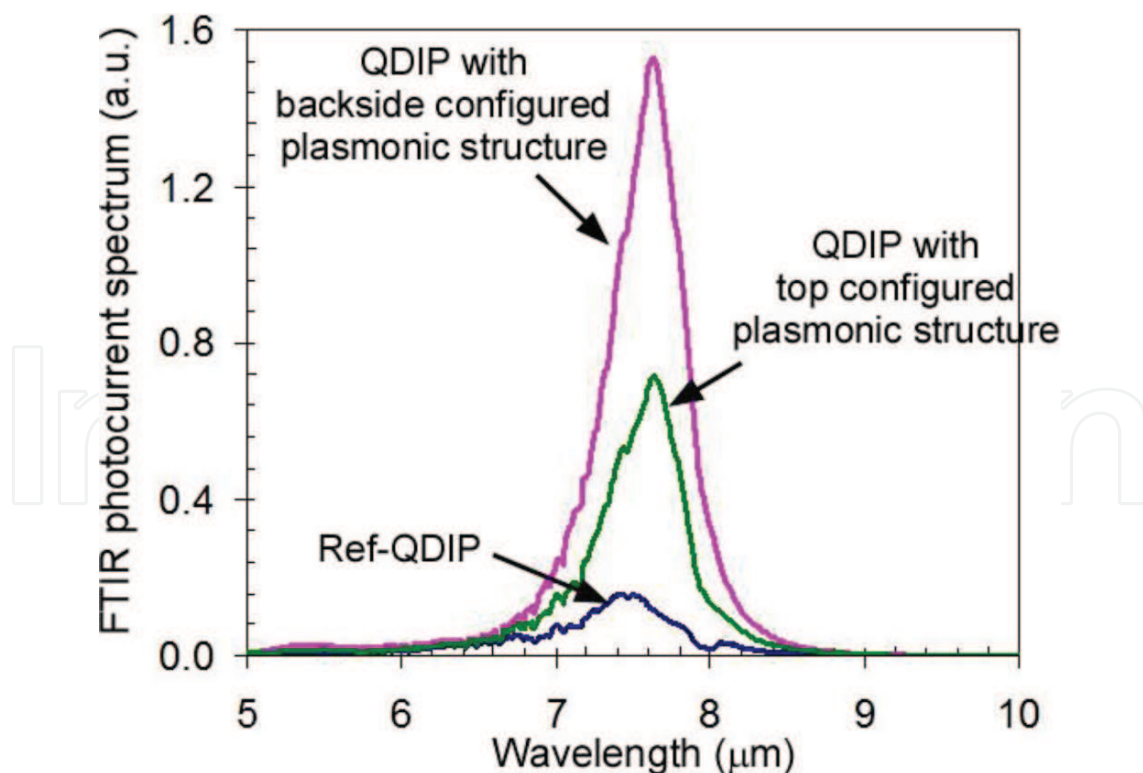


**Figure 9.** Measured photocurrent spectra of the backside-configured plasmonic QDIP compared with the top-side configured plasmonic QDIP and the reference QDIP. The backside-configured plasmonic QDIP clearly shows higher plasmonic enhancement.

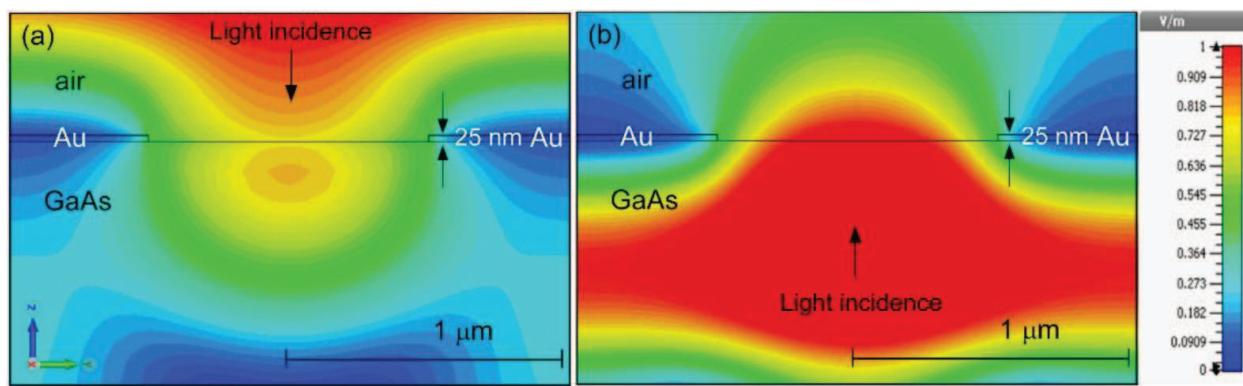


**Figure 10.** Simulated E-field intensities: (a) top-configured plasmonic structure and (b) backside-configured plasmonic structure. The backside-configured plasmonic structure can induce stronger E-field at the interface and therefore can provide larger plasmonic enhancement (© IOP Publishing. Reproduced with permission from Ref. [12]. All rights reserved).

peaks  $\lambda_{sp}$  of different  $(m, n)$  orders for various 2DSHA periods  $p$  are shown in **Figure 11** that exhibits the linear dependence of the resonant peak wavelength  $\lambda_{sp}$  with the period  $p$  of the 2DSHA for different  $(m, n)$  orders. As predicted by Eq. (43), good linearity is obtained for both the  $(1, 0)$ th or  $(0, 1)$ th and the  $(1, 1)$ th order plasmonic resonant peaks.

We define the photocurrent enhancement ratio  $R$  as follows:

$$R = \frac{I_{\text{plasmonic}}}{I_{\text{ref}}} \quad (44)$$

where  $I_{\text{plasmonic}}$  is the photocurrent of the plasmonic QDIP and  $I_{\text{ref}}$  is the photocurrent of the reference QDIP without the 2DSHA structures.

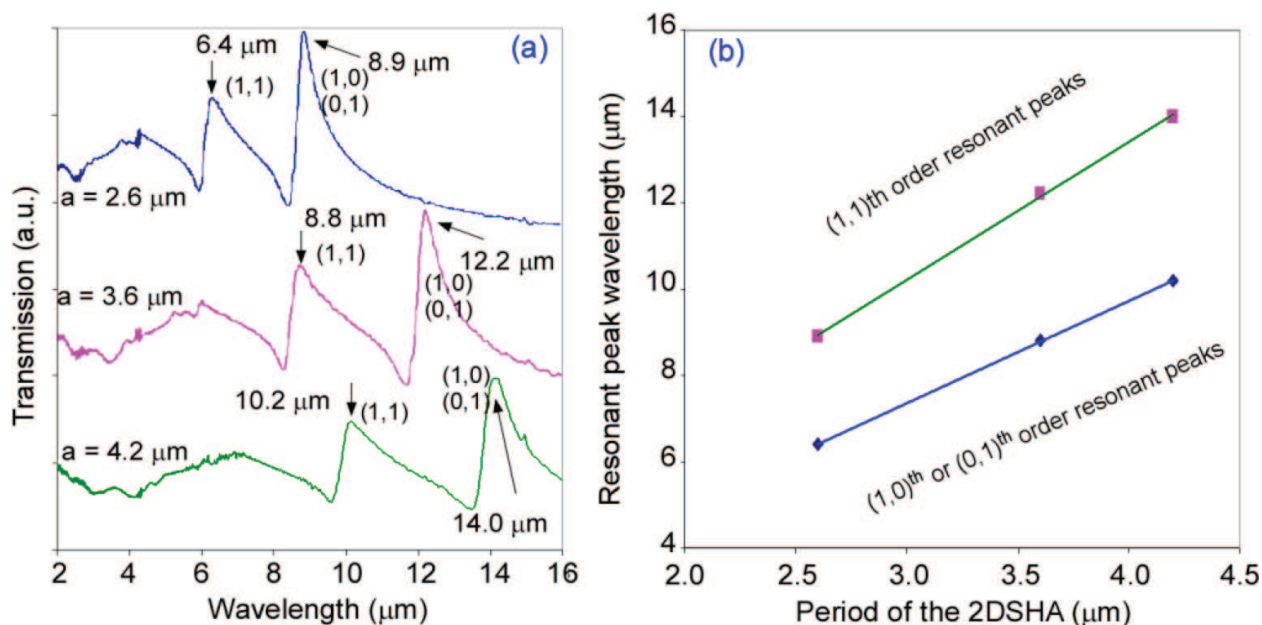


**Figure 11.** (a) Plasmonic resonant peaks  $\lambda_{sp}$  of different  $(i, j)$  orders for various 2DSHA periods; (b) linear dependence of the resonant peak wavelength  $\lambda_{sp}$  with the period of different  $(m, n)$  orders.



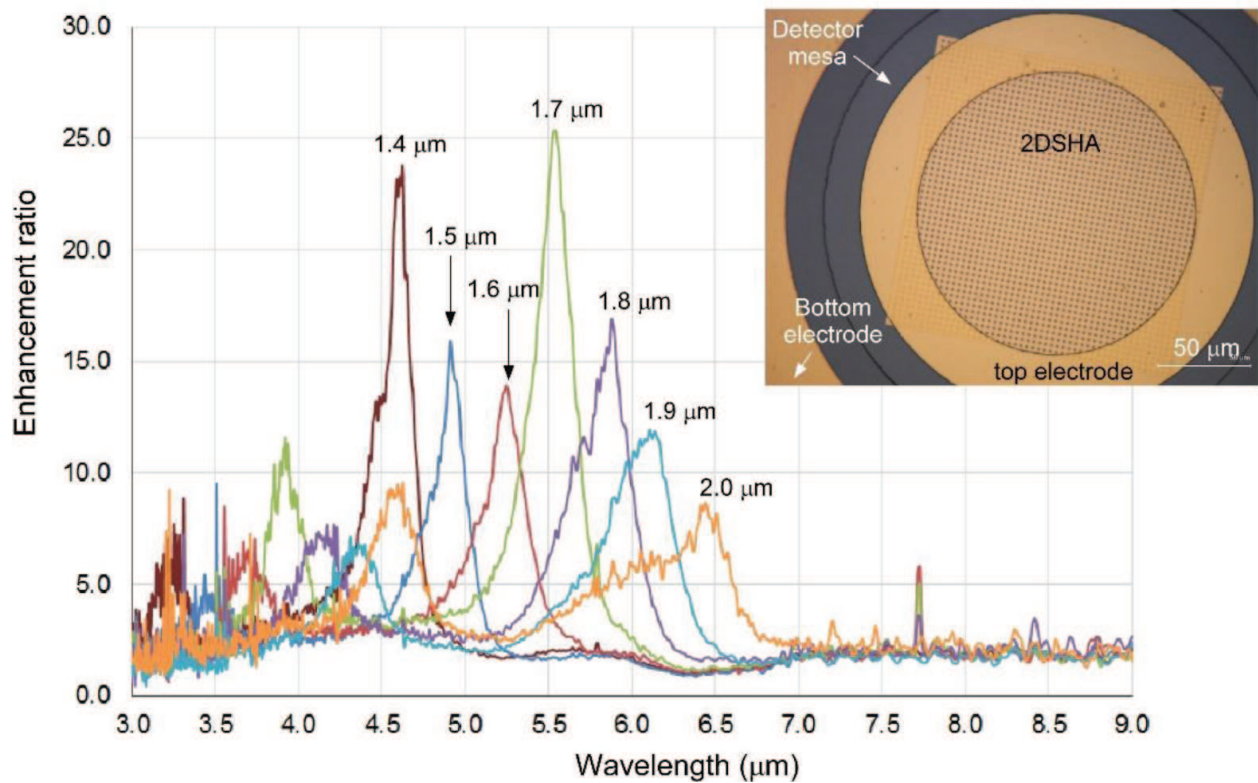


**Figure 12.** Photocurrent enhancement ratio spectra for plasmonic QDIPs with different periods varying from 1.4 to 2.0  $\mu\text{m}$ . The insert is a microscopic picture of a QDIP with a 2DSHA plasmonic structure (Reproduced from Ref. [28] with the permission of AIP Publishing).

**Figure 12** shows the photocurrent enhancement ratio spectra for all the plasmonic QDIPs with different periods from 1.4 to 2.0  $\mu\text{m}$ . The periods of the 2DSHA plasmonic structures are marked on the curves. The insert shows a microscopic picture of a QDIP with a 2DSHA plasmonic structure. The IR incidence is from the backside of the QDIPs, that is, backside-configured 2DSHA plasmonic structures.

As shown in **Figure 12**, the enhancement wavelengths can be tuned by varying the periods of the 2DSHA plasmonic structures. This allows one to achieve multispectral QDIPs without fabricating an individual filter on each photodetector [28].

#### 4.3. Polarization dependence and polarimetric detection

From Eq. (43), the plasmonic resonant wavelength depends on the period  $p$ . By changing the plasmonic lattice from a square lattice to a rectangular lattice with different periods in the  $x$  and  $y$  directions, one can engineer the resonant wavelengths at different polarizations.

**Figure 13(a)** shows an SEM picture of a rectangular lattice 2DSHA plasmonic structure with the periods of 2.6 and 3.0  $\mu\text{m}$  in the  $x$ -direction and the  $y$ -direction, respectively. **Figure 13(b)–(d)** shows the transmission spectra of the un-polarized, 90° polarized (i.e. polarization in  $y$ -direction), and 0° polarized (i.e. polarization in  $x$ -direction), respectively. The resonant wavelengths correspond to the orders in the  $x$ - and  $y$ - directions are marked in the figures. The un-polarized light shows transmission in both (0, 1) and (1, 0) orders. However, the 0° polarized

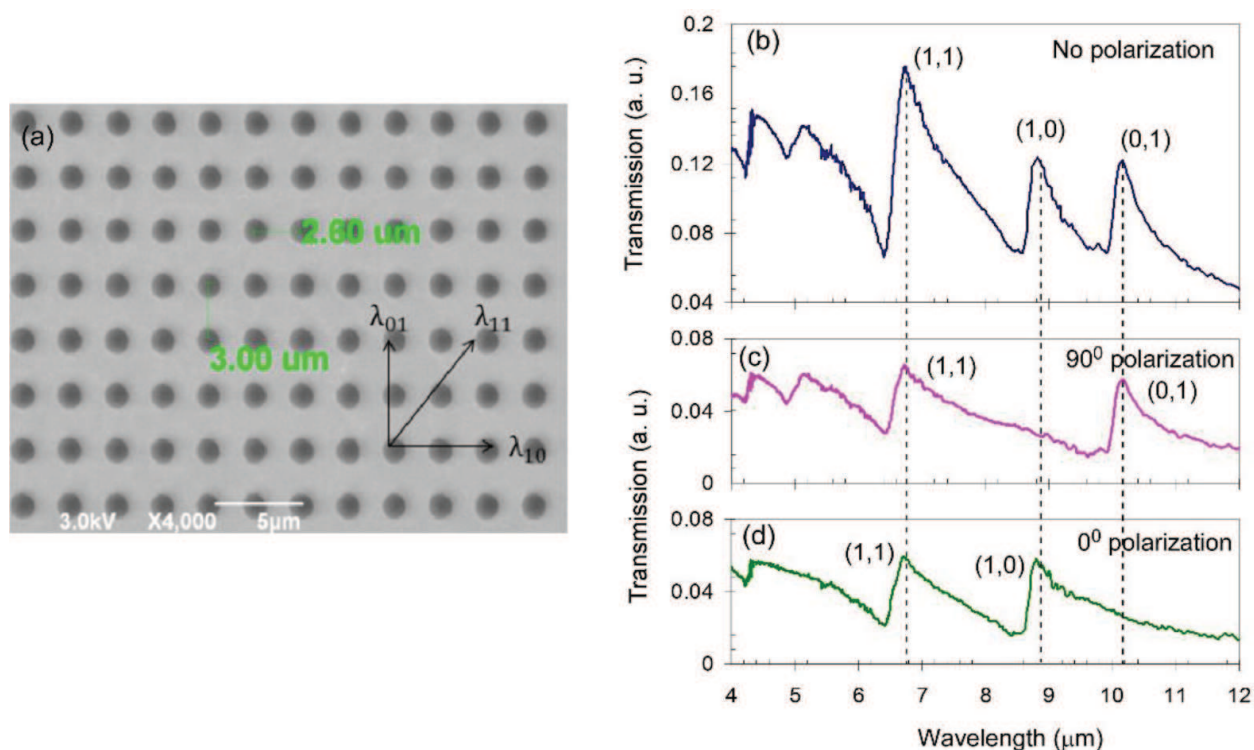


**Figure 13.** (a) SEM picture of rectangular lattice 2DSHA structure. The periods in  $x$ - and  $y$ - directions are 2.6 and 3.0 μm, respectively. (b), (c) and (d) transmission spectra at of the un-polarized, 90° polarized (i.e. polarization in  $y$ -direction), and 0° polarized (i.e. polarization in  $x$ -direction), respectively. The polarized light only shows transmission at their corresponding resonant wavelengths (© IOP Publishing. Reproduced with permission from Ref. [11]. All rights reserved).

light only shows transmission at the (1, 0) order resonant wavelength and the 90° polarized light only shows transmission at the (0, 1) order.

**Figure 14** shows a microscopic picture of a QDIP with the rectangular lattice 2DSHA structure. The insert shows an SEM picture of the rectangular lattice 2DSHA structure.

**Figure 15(a)** and **(b)** shows the measured detection spectra of the plasmonic QDIP at 90° polarization and 0° polarization, respectively. The photo-response of a reference QDIP without the plasmonic structure is also shown in the figures for comparison. The plasmonic QDIP shows different detection wavelengths at different polarizations.

#### 4.4. Angular dependence of the 2DSHA plasmonic enhancement

**Figure 16** shows the schematic view of the top-illuminated 2DSHA plasmonic QDIP with an incident angle  $\theta$ .

From Eq. (41), the coupling efficiency  $\eta$  to the plasmonic waves depends on the overlap integral of  $H(x, z)$  with the plasmonic wave  $e^{i(k_{spp}x + k_{2z}z)}$ . At the incident angle  $\theta$ , the  $H(x, z)$  not only periodically modulated by the 2DSHA structure, but also added additional phase term  $e^{i(k_0 \sin \theta x)}$ , that is,



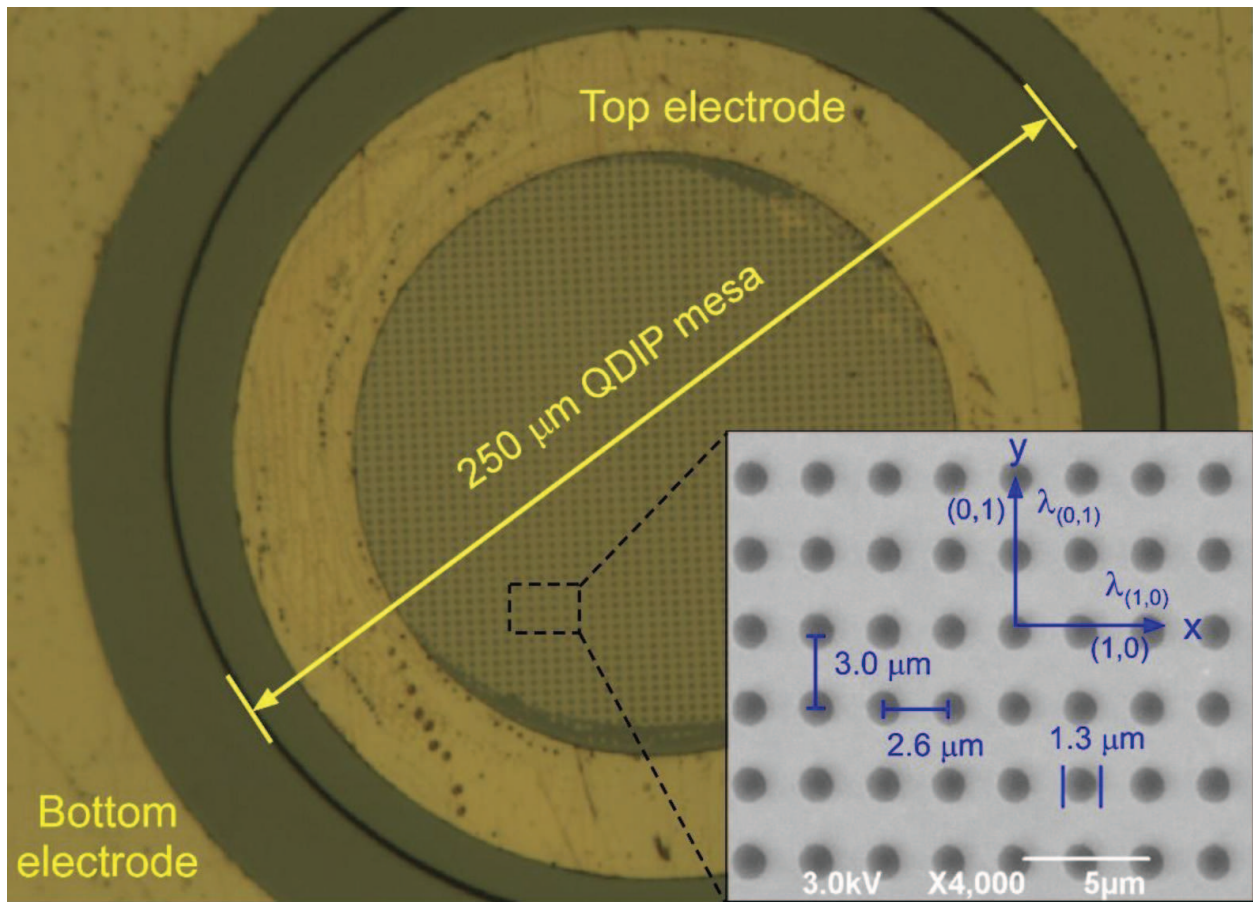


**Figure 14.** Microscopic picture of a QDIP with the rectangular lattice 2DSHA structure. Insert: SEM picture of the rectangular lattice 2DSHA structure (© IOP Publishing. Reproduced with permission from Ref. [11]. All rights reserved).

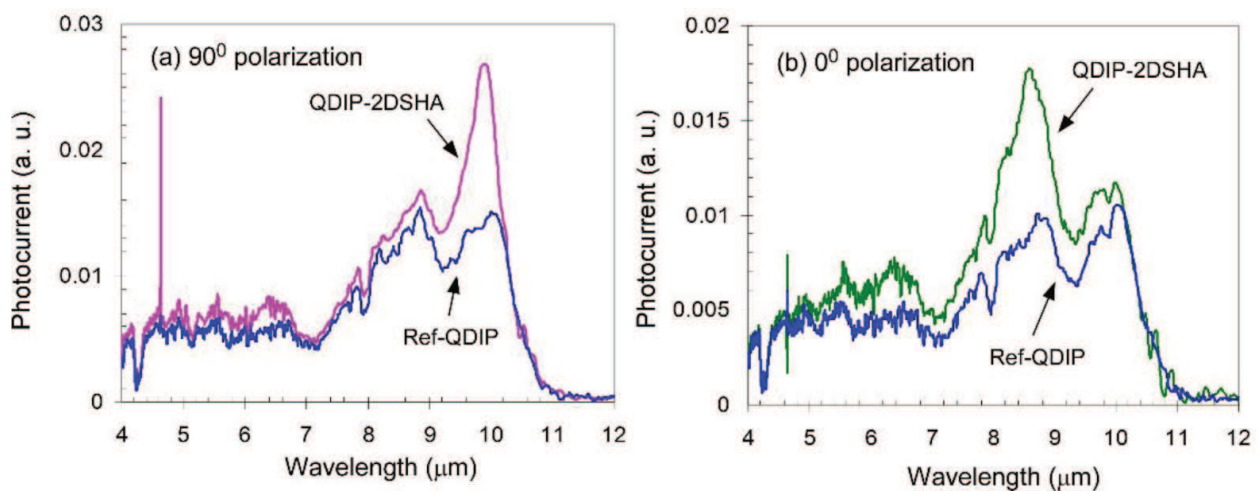


**Figure 15.** Measured detection spectra of the plasmonic QDIP at different polarizations: (a)  $90^\circ$  polarization and (b)  $0^\circ$  polarization. Different polarizations show different detection wavelengths (© IOP Publishing. Reproduced with permission from Ref. [11]. All rights reserved).

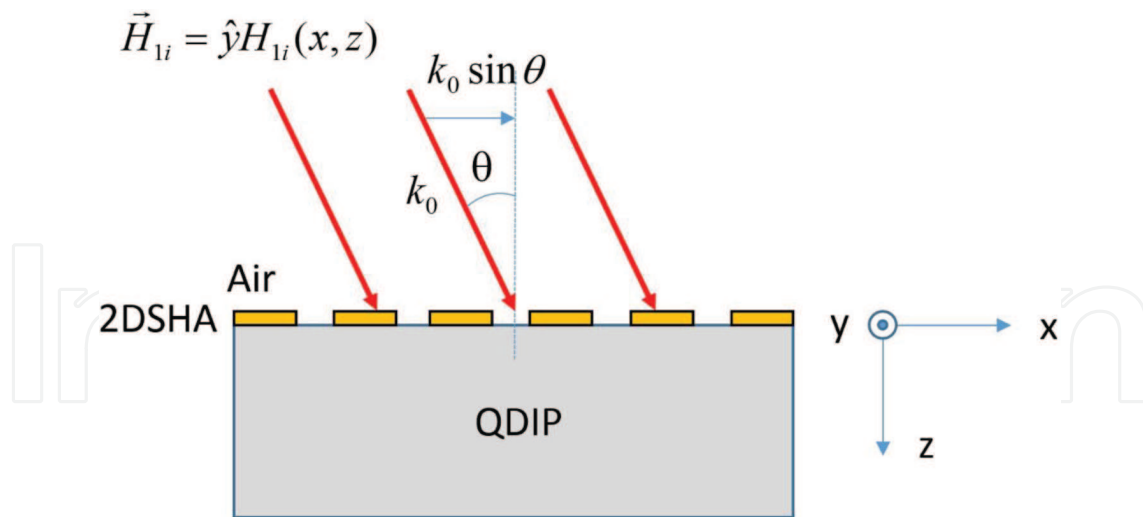


Figure 16. Schematic view of the top-illuminated 2DSHA plasmonic QDIP with an incident angle  $\theta$ .

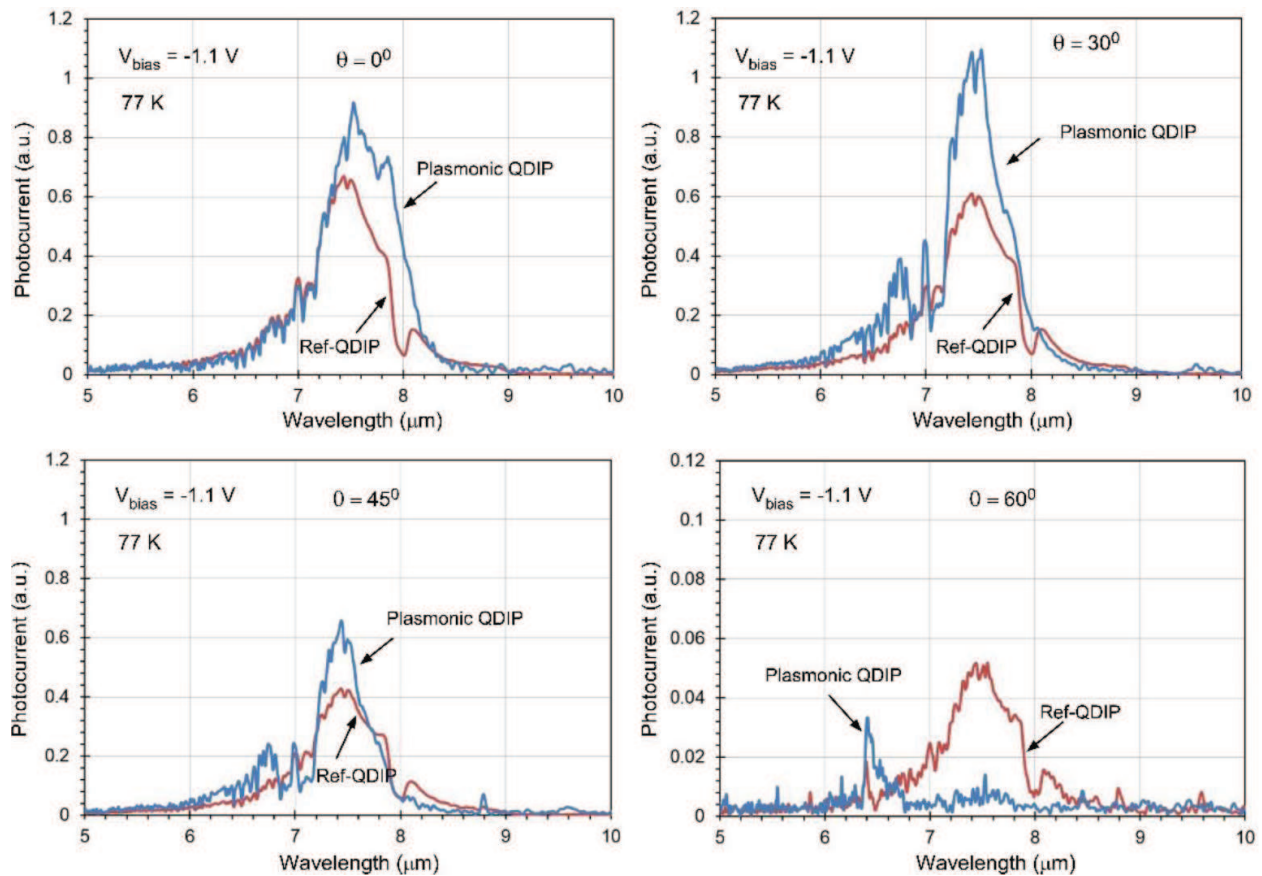


Figure 17. Measured photocurrent of the 2DSHA plasmonic QDIP at different incident angles of  $0^\circ$ ,  $30^\circ$ ,  $45^\circ$  and  $60^\circ$  compared with the reference QDIP at the same incident angles. The plasmonic resonant wavelength  $\lambda_0$  shift to shorter wavelengths as the incident angle increases.

$$H(x, z) \propto e^{\pm i\Lambda x} e^{ik_0 \sin\theta x} \quad (45)$$

From Eq. (45), the coupling condition can be expressed as follows:

$$k_0 \sin\theta \pm \Lambda = k_{spp} \quad (46)$$

Taking the + sign, one can write Eq. (46) in terms of plasmonic resonant wavelength  $\lambda_0$  as follows:

$$\lambda_0 = \left\{ \text{Re} \left[ \sqrt{\frac{\epsilon_{2cr} \epsilon_{1r}}{(\epsilon_{1r} + \epsilon_{2cr})}} - \sin\theta \right] \right\} \Lambda \quad (47)$$

Eq. (47) shows that the enhancement wavelength shifts to shorter wavelengths as the incident angle increases.

**Figure 17** shows the measured photocurrent of the 2DSHA plasmonic QDIP at different incident angles of  $0^\circ$ ,  $30^\circ$ ,  $45^\circ$ , and  $60^\circ$  compared with the reference QDIP at the same incident angles. Blue shift of the plasmonic resonant wavelengths  $\lambda_0$  is experimentally observed as the incident angle increases.

To quantitatively analyse the relationship between the plasmonic wavelength shift and the incident angle, we plot the plasmonic resonant wavelengths  $\lambda_0$  versus  $\sin\theta$ . **Figure 18** shows the  $\lambda_0$  versus  $\sin\theta$ . A linear relation is obtained, which agrees well with Eq. (47). The interception and the slope are  $7.6$  and  $-1.4 \mu\text{m}$ , respectively. The interception  $7.6 \mu\text{m}$  matches the value

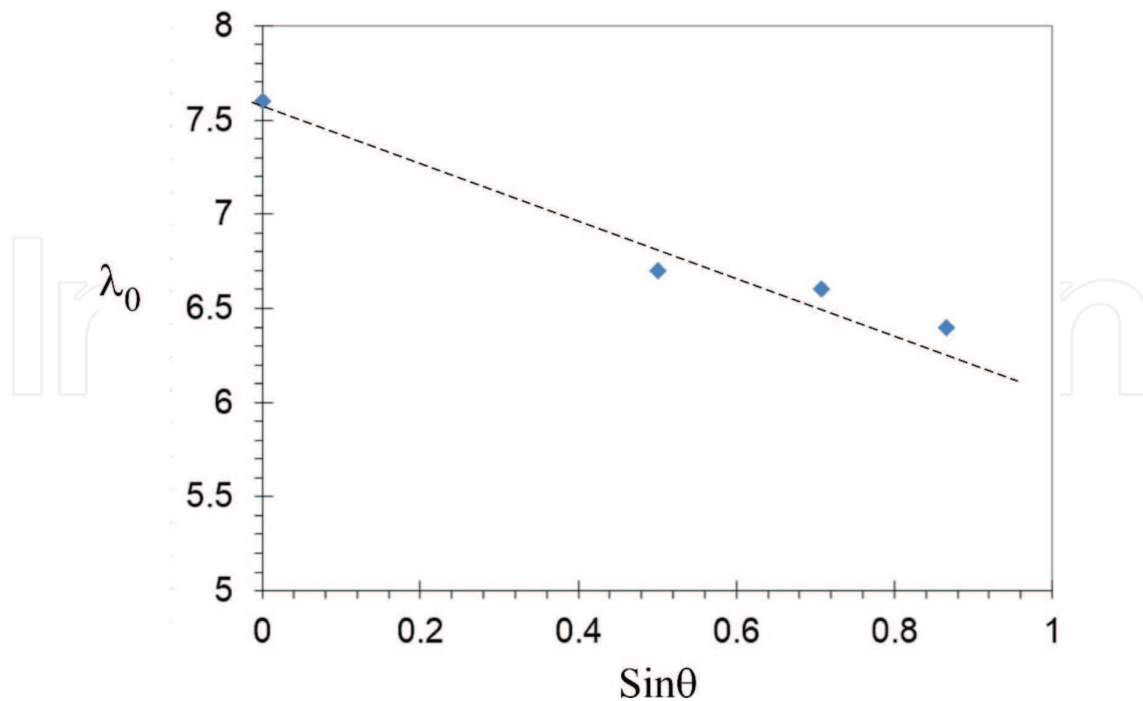


**Figure 18.**  $\lambda_0$  versus  $\sin\theta$  plot.  $\lambda_0$  varies linearly with  $\sin\theta$ . The interception and the slope are  $7.6$  and  $-1.4 \mu\text{m}$ , respectively.

$Re\left[\sqrt{\frac{\epsilon_{2cr}\epsilon_{1r}}{\epsilon_{1r}+\epsilon_{2cr}}}\right]\Lambda$  in Eq. (47). However, the slope of  $-1.4 \mu\text{m}$  is smaller than  $\Lambda = 2.3 \mu\text{m}$  as predicted in Eq. (47). This may be due to the plasmonic scattering-induced phase distribution in  $H(x, z)$  in addition to the  $e^{i(k_0 \sin \theta x)}$  term.

## 5. Conclusion

In conclusion, 2D SHA plasmonic structures can effectively induce plasmonic resonant waves. The resonant wavelength depends on the period of the plasmonic structure. The surface confinement effect allows one to improve the performance of QDIPs. The plasmonic enhancement also strongly depends on the polarization and the incident angle. The polarization and incident angle dependence allow polarimetric and polarization engineering in QDIP designs.

## Author details

Guiru Gu<sup>1\*</sup>, Xuejun Lu<sup>2</sup>, Thitikorn Kemsri<sup>2</sup> and Yingjie Zhang<sup>2</sup>

\*Address all correspondence to: ggu@stonehill.edu

1 Stonehill College, Easton, MA, USA

2 University of Massachusetts Lowell, Lowell, MA, USA

## References

- [1] R. H. Ritchie, "Plasma losses by fast electrons in thin films," *Physical Review*, vol. 106, pp. 874–881, 06/01/1957.
- [2] H. Raether, *Surface Plasmons on Smooth Surfaces*. Springer, Berlin Heidelberg, 1988.
- [3] K. Kneipp, Y. Wang, H. Kneipp, L. T. Perelman, I. Itzkan, R. R. Dasari, *et al.*, "Single molecule detection using surface-enhanced Raman scattering (SERS)," *Physical Review Letters*, vol. 78, pp. 1667–1670, 03/03/1997.
- [4] S. Nie and S. R. Emory, "Probing single molecules and single nanoparticles by surface-enhanced Raman scattering," *Science*, vol. 275, pp. 1102–1106, 1997.
- [5] K. Kneipp and H. Kneipp, "SERS signals at the anti stokes side of the excitation laser in extremely high local optical fields of silver and gold nanoclusters," *Faraday Discuss*, vol. 132, pp. 27–33; discussion 85–94, 2006.
- [6] K. A. Willets and R. P. Van Duyne, "Localized surface plasmon resonance spectroscopy and sensing," *Annual Review of Physical Chemistry*, vol. 58, pp. 267–297, 2007.



- [7] H. Xu, E. J. Bjerneld, M. Käll, and L. Börjesson, "Spectroscopy of single hemoglobin molecules by surface enhanced Raman scattering," *Physical Review Letters*, vol. 83, pp. 4357–4360, 11/22/1999.
- [8] C.-C. Chang, Y. D. Sharma, Y.-S. Kim, J. A. Bur, R. V. Shenoi, S. Krishna, *et al.*, "A surface plasmon enhanced infrared photodetector based on InAs quantum dots," *Nano Letters*, vol. 10, pp. 1704–1709, 2010.
- [9] P. Senanayake, C.-H. Hung, J. Shapiro, A. Lin, B. Liang, B. S. Williams, *et al.*, "Surface plasmon-enhanced nanopillar photodetectors," *Nano Letters*, vol. 11, pp. 5279–5283, 2011.
- [10] P. Vasinajindakaw, J. Vaillancourt, G. Gu, R. Liu, Y. Ling, and X. Lu, "A Fano-type interference enhanced quantum dot infrared photodetector," *Applied Physics Letters*, vol. 98, pp. 211111–1 to 211111–3, 2011.
- [11] P. Vasinajindakaw, J. Vaillancourt, G. Gu, and X. Lu, "Surface plasmonic enhanced polarimetric longwave infrared photodetection with band pass spectral filtering," *Semiconductor Science and Technology*, vol. 27, pp. 65005–65009, 2012. <http://dx.doi.org/10.1088/0268-1242/27/6/065005>.
- [12] G. Gu, J. Vaillancourt, P. Vasinajindakaw, and X. Lu, "Backside-configured surface plasmonic structure with over 40 times photocurrent enhancement," *Semiconductor Science and Technology*, vol. 28, p. 105005, 2013. <http://dx.doi.org/10.1088/0268-1242/28/10/105005>.
- [13] G. Gu, N. Mojaverian, J. Vaillancourt, and X. Lu, "Surface plasmonic resonance induced near-field vectors and their contribution to quantum dot infrared photodetector enhancement," *Journal of Physics D: Applied Physics*, vol. 47, p. 435106, 2014.
- [14] G. Gu, J. Vaillancourt, and X. Lu, "Analysis of near-field components of a plasmonic optical antenna and their contribution to quantum dot infrared photodetector enhancement," *Optics Express*, vol. 22, pp. 24970–24976, 2014/10/20 2014.
- [15] J. Vaillancourt, N. Mojaverian, and L. Xuejun, "A longwave infrared focal plane array enhanced by backside-configured plasmonic structures," *IEEE Photonics Technology Letters*, vol. 26, pp. 745–748, 2014.
- [16] R. Liu, P. Vasinajindakaw, G. Gu, J. Vaillancourt, and X. Lu, "Optimizing light absorption in quantum dot infrared photodetectors by tuning surface confinement of surface plasmonic waves," *Journal of Physics D: Applied Physics*, vol. 46, p. 015102, 2013.
- [17] P. Drude, "Electron theory of metals," *Annalen der Physik*, vol. 306, pp. 566–613, 1900.
- [18] T. W. Ebbesen, H. Lezec, H. Ghaemi, T. Thio, and P. Wolff, "Extraordinary optical transmission through sub-wavelength hole arrays," *Nature*, vol. 391, pp. 667–669, 1998.
- [19] *Handbook of Optical Constants of Solids*. Academic Press, San Diego London New York Boston Sydney Tokyo Toronto, 1998.

- [20] D. Pan, E. Towe, and S. Kennerly, "Normal-incidence intersubband (In, Ga)As/GaAs quantum dot infrared photodetectors," *Applied Physics Letters*, vol. 73, pp. 1937–1939, 1998.
- [21] H. C. Liu, M. Gao, J. McCaffrey, Z. R. Wasilewski, and S. Fafard, "Quantum dot infrared photodetectors," *Applied Physics Letters*, vol. 78, pp. 79–81, 2001.
- [22] A. D. Stiff, S. Krishna, P. Bhattacharya, and S. Kennerly, "High-detectivity, normal-incidence, mid-infrared ( $\lambda \sim 4 \mu\text{m}$ ) InAs/GaAs quantum-dot detector operating at 150 K," *Applied Physics Letters*, vol. 79, pp. 421–423, 2001.
- [23] L. Jiang, S. S. Li, N.-T. Yeh, J.-I. Chyi, C. E. Ross, and K. S. Jones, "In<sub>0.6</sub>Ga<sub>0.4</sub>As/GaAs quantum-dot infrared photodetector with operating temperature up to 260 K," *Applied Physics Letters*, vol. 82, pp. 1986–1988, 2003.
- [24] S. Krishna, S. Raghavan, G. v. Winckel, P. Rotella, A. Stintz, C. P. Morath, *et al.*, "Two color InAs/InGaAs dots-in-a-well detector with background-limited performance at 91 K," *Applied Physics Letters*, vol. 82, pp. 2574–2576, 2003.
- [25] S. Chakrabarti, A. D. Stiff-Roberts, P. Bhattacharya, S. Gunapala, S. Bandara, S. B. Rafol, *et al.*, "High-temperature operation of InAs-GaAs quantum-dot infrared photodetectors with large responsivity and detectivity," *Photonics Technology Letters, IEEE*, vol. 16, pp. 1361–1363, 2004.
- [26] J. C. Campbell and A. Madhukar, "Quantum-dot infrared photodetectors," *Proceedings of the IEEE*, vol. 95, p. 1815, 2007.
- [27] X. Lu, J. Vaillancourt, and M. J. Meisner, "Temperature-dependent photoresponsivity and high-temperature (190K) operation of a quantum dot infrared photodetector," *Applied Physics Letters*, vol. 91, pp. 051115–1 to 051115–3, 2007.
- [28] Y. Zhang, J. Vaillancourt, G. Gu, W. Guo, and X. Lu, "Quantum selection rule dependent plasmonic enhancement in quantum dot infrared photodetectors," *Journal of Applied Physics*, vol. 119, p. 193103, 2016. <http://dx.doi.org/10.1063/1.4949511>.

IntechOpen

